PAPER • OPEN ACCESS

Results from recent detachment experiments in alternative divertor configurations on TCV

To cite this article: C. Theiler *et al* 2017 *Nucl. Fusion* **57** 072008

OPEN ACCESS
IOP Publishing | International Atomic Energy Agency
Nuclear Fusion
Nucl. Fusion **57** (2017) 072008 (16pp)
https://doi.org/10.1088/1741-4326/aa5fb7

Results from recent detachment experiments in alternative divertor configurations on TCV

C. Theiler[1], B. Lipschultz[2], J. Harrison[3], B. Labit[1], H. Reimerdes[1], C. Tsui[1,4], W.A.J. Vijvers[5], J. A. Boedo[4], B.P. Duval[1], S. Elmore[3], P. Innocente[6], U. Kruezi[3], T. Lunt[7], R. Maurizio[1], F. Nespoli[1], U. Sheikh[1], A.J. Thornton[3], S.H.M. van Limpt[5], K. Verhaegh[1,2], N. Vianello[6] the TCV team and the EUROfusion MST1 team[a]

[1] Swiss Plasma Center (SPC), Ecole Polytechnique Fédérale de Lausanne (EPFL), CH-1015 Lausanne, Switzerland
[2] York Plasma Institute, Department of Physics, University of York, Heslington, York, YO10 5DD, United Kingdom
[3] CCFE, Culham Science Centre, Abingdon, Oxon, OX14 3DB, United Kingdom
[4] University of California San Diego (UCSD), San Diego, CA, United States of America
[5] DIFFER - Dutch Institute for Fundamental Energy Research, De Zaale 20, 5612 AJ Eindhoven, the Netherlands
[6] Consorzio RFX, Corso Stati Uniti 4, 35127 Padova, Italy
[7] Max Planck Institut für Plasmaphysik, Boltzmannstr. 2, 85748 Garching, Germany

E-mail: christian.theiler@epfl.ch

Received 15 September 2016, revised 28 January 2017
Accepted for publication 9 February 2017
Published 21 March 2017

Abstract

Divertor detachment is explored on the TCV tokamak in alternative magnetic geometries. Starting from typical TCV single-null shapes, the poloidal flux expansion at the outer strikepoint is varied by a factor of 10 to investigate the X-divertor characteristics, and the total flux expansion is varied by 70% to study the properties of the super-X divertor. The effect of an additional X-point near the target is investigated in X-point target divertors. Detachment of the outer target is studied in these plasmas during Ohmic density ramps and with the ion ∇B drift away from the primary X-point. The detachment threshold, depth of detachment, and the stability of the radiation location are investigated using target measurements from the wall-embedded Langmuir probes and two-dimensional CIII line emissivity profiles across the divertor region, obtained from inverted, toroidally-integrated camera data. It is found that increasing poloidal flux expansion results in a deeper detachment for a given line-averaged density and a reduction in the radiation location sensitivity to core density, while no large effect on the detachment threshold is observed. The total flux expansion, contrary to expectations, does not show a significant influence on any detachment characteristics in these experiments. In X-point target geometries, no evidence is found for a reduced detachment threshold despite a

[a] See the author list of 'Overview of progress in European Medium Sized Tokamaks towards an integrated plasma-edge/wall solution' by H. Meyer *et al*, to be published in the *Nuclear Fusion* special issue: Overview and Summary Reports from the 26th Fusion Energy Conference (Kyoto, Japan, 17–22 October 2016)

2–3 fold increase in connection length. A reduced radiation location sensitivity to core plasma density in the vicinity of the target X-point is suggested by the measurements.

Keywords: detachment, alternative divertors, X-divertor, super-X divertor, X-point target divertor

(Some figures may appear in colour only in the online journal)

1. Introduction

In magnetic confinement devices for fusion, such as tokamaks, plasma thermal energy constantly enters the scrape-off layer (SOL) via cross-field transport from the confined plasma. In the SOL, most of this exhaust heat is transported along a narrow layer towards localised regions of the surrounding vacuum vessel. If unmitigated, the resulting steady-state heat fluxes will exceed the material limits of $\approx$10 MWm^{-2} in ITER size devices [1] and even more so in a demonstration fusion power plant (DEMO) [2, 3]. An additional concern is long-term erosion due to sputtering. Assuming that tungsten is the wall material, electron temperatures near the wall of $\lesssim$5 eV are required to keep erosion (mainly due to tungsten sputtering by impurities) at acceptable levels [4–7]—a strong contrast to the temperatures of 100 eV and more in the SOL region adjacent to the confined plasma.

In divertor geometries, a magnetic X-point is introduced which diverts plasma-wall interaction to dedicated wall structures, the target or divertor plates, located somewhat remotely from the core plasma. The divertor configuration is key for efficient pumping of the particle exhaust, to limit the influx of impurities released at the plasma-wall interface, and to access high-confinement regimes [8, 9]. The divertor configuration also allows for some peak target heat flux reduction by cross-field transport in the divertor leg between the X-point and the target. More importantly, however, it allows for substantial temperature gradients along the magnetic field from the upstream SOL to the plate. As a result, different volumetric processes can occur in the divertor, which distribute the exhaust heat over a larger area, reducing peak heat fluxes to the wall [10]. In the range of 10 eV to a few tens of eV, low-Z impurities can efficiently radiate power in an isotropic manner [4]. Once electron temperatures drop below approximately 5 eV, neutrals can drag away the energy and momentum of the ions via charge exchange reactions. The result is an additional spreading of the power footprint as well as a loss of plasma pressure along the magnetic field. This process of plasma detachment is amplified at temperatures below approximately 1 eV by volumetric recombination. To access detachment in high heat flux conditions with sufficiently high radiated power fractions ($\geqslant$60% in ITER and $\geqslant$95% in DEMO [3, 11]) requires intense impurity seeding levels. Access to detachment is also known to be facilitated by an increase in divertor neutral pressure, achieved by divertor baffling (e.g. in vertical plate divertors [9]).

While a detached divertor is extremely beneficial in terms of target heat fluxes and erosion issues, too high levels of detachment can be problematic for the core plasma. The cold, radiative region can move to the X-point and into the core plasma, often affecting core confinement and impurity and neutral compression in the divertor [9, 12]. Therefore, ITER plans to operate with a partially detached divertor [13, 14], where only the part of the strikepoint close to the separatrix is detached. Quantitative performance predictions are difficult and whether such a solution is viable for a DEMO is currently unclear.

Due to the enormous challenge of developing a viable exhaust solution, detachment is being studied extensively in conventional divertors with promising recent results from metal machines also in fully detached divertor operation [3], [15–18]. In parallel, alternative divertor configurations, mainly based on more complex magnetic geometries, are being explored both experimentally and theoretically (see, e.g. [19–22] and [23, 24]). Among the most prominent ones are the snowflake divertor (SF) [25], the X-divertor (XD) [26, 27], the super-X divertor (SXD) [28], and the X-point target divertor (XPT) [29]. The expected benefits of these geometries include easier access to detachment (e.g. requiring lower impurity seeding levels), higher total power dissipation capabilities, and better control over the location of the radiation front [29–31]. Besides providing a potential backup solution for the case where the conventional divertor does not extrapolate to a reactor, studying these configurations is important in order to develop a better understanding of edge turbulence and detachment physics.

In this paper, we present the initial results of a fundamental study of the impact of the magnetic configuration on the detachment behavior in newly developed alternative divertor shapes in the all-carbon device TCV and for low power, Ohmic conditions. Focusing on the outer divertor leg, we explore the XD and SXD properties by scanning poloidal and total flux expansion. We also study the effect of an additional X-point near the target in XPTs. The rest of the paper is organised as follows. In section 2, we discuss heat exhaust and its dependence on geometry more quantitatively and discuss the potential benefits of different geometrical aspects of advanced divertors. In section 3, we present the experimental setup together with basic aspects of the detachment behaviour in a specific geometry. In this section, we also introduce the diagnostic tools which are employed subsequently to explore detachment in XDs (section 4), SXDs (section 5) and XPTs (section 6). A summary and conclusions are presented in section 7.

2. Potential benefits of alternative divertor geometries

We discuss here potential benefits of alternative divertor magnetic geometries in terms of detachment behavior and heat exhaust and start with the possibility of reducing peak heat

fluxes by geometrical means in the absence of cross-field transport and volumetric power losses. We focus on the outer divertor leg and refer to the situation sketched in figure 1(*a*) (the inner divertor is quickly discussed at the end of this section). We consider the volume between two closely (infinitesimally) spaced flux surfaces in the SOL with an upstream separation of Δr^u. For simplicity, we assume that all the power enters the SOL at the outboard midplane and we denote the resulting upstream poloidal heat flux towards the outer target with q_θ^u.

To increase the area onto which heat is deposited and hence to reduce the resulting heat flux perpendicular to the divertor plate, $q_\perp^t$, one possibility is to tilt the divertor plate in the poloidal plane by an angle β, as shown in figure 1(*a*). An alternative is to increase the spacing between the flux surfaces at the plate, as illustrated in figure 1(*b*). This is termed *poloidal flux expansion*, f_x, which we define here as the ratio of the perpendicular flux surface spacing at the target and upstream. f_x can then be written as

$$f_x = \frac{\Delta r^t}{\Delta r^u} = \frac{B_\theta^u R_u}{B_\theta^t R_t} = \frac{B_\theta^u B_\phi^t}{B_\theta^t B_\phi^u}. \tag{1}$$

Here, u and t denote upstream and target quantities, θ and ϕ denote poloidal and toroidal components of the magnetic field, and R is the major radius. Finally, a third option to reduce $q_\perp^t$ is to bring the outer strikepoint (OSP) to a larger major radius, as illustrated in figure 1(*c*).

Assuming toroidal symmetry, we can immediately write $q_\perp^t$ as follows

$$q_\perp^t = \frac{R_u}{R_t}\frac{\sin\beta}{f_x} q_\theta^u, \tag{2}$$

which takes into account the three effects for heat flux reduction: wall tilt, poloidal flux expansion, and an increase of the target major radius.

Based on the definition of f_x in equation (1) and simple geometrical considerations, one can show that both flux expansion and wall tilt reduce the total grazing incidence angle between the magnetic field and divertor plate, which we denote by α. Indeed, one can write

$$\begin{aligned}\frac{\sin\beta}{f_x} &= \tan\alpha \cdot \frac{B_\phi^u}{B_\theta^u} \cdot \sqrt{\frac{(B_\phi^t)^2 + (\cos\beta \cdot B_\theta^t)^2}{(B_\phi^t)^2}} \\ &\approx \tan\alpha \cdot \frac{B_\phi^u}{B_\theta^u}.\end{aligned} \tag{3}$$

Due to engineering constraints, there is, at least in the attached conditions considered here, a lower limit to the achievable values of the angle α and hence also on the possible heat flux reduction by wall tilt and/or poloidal flux expansion.

It is worth mentioning here that wall tilt and poloidal flux expansion do not, to leading order, change, $q_\parallel$, the heat flux parallel to the magnetic field. The reduction in $q_\perp^t$ is caused by a reduction of the incidence angle α on the wall. The situation is different when R_t is varied. In this case, the total magnetic field $B \approx B_\phi \propto 1/R_t$ is varied significantly. The result is *total flux expansion*, i.e. the increase of the cross-section area of a flux tube, which scales as $1/B$. As a result, to keep the power along the flux tube constant, $q_\parallel$ varies proportionally to B.

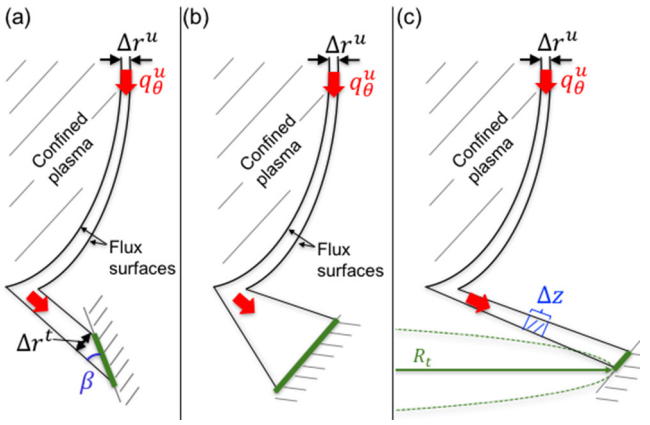

Figure 1. Sketches of heat transport between two closely spaced flux surfaces in the SOL from the outer midplane to the outer target, illustrating peak heat flux reduction by purely geometrical means. (*a*) By poloidal wall tilt, (*b*) by poloidal flux expansion $f_x = \Delta r^t/\Delta r^u$, and (*c*) by an increase in the strikepoint major radius R_t.

We now consider again equation (2). If we assume an exponentially decaying radial profile for q_θ^u with e-folding length λ_q and if f_x and β do not vary too strongly along the divertor plate, the peak target heat flux (still assuming purely parallel transport from the midplane to the plate) is at the strikepoint and can be written as

$$q_{\perp,\mathrm{peak}}^t = \frac{P_{\mathrm{div}}}{2\pi R_t \lambda_q}\frac{\sin\beta}{f_x} \tag{4}$$

$$\approx \frac{P_{\mathrm{div}}}{2\pi R_t \lambda_q} \cdot \frac{B_\phi^u}{B_\theta^u}\tan\alpha. \tag{5}$$

Here, P_{div} is the total power to the OSP and we have used equation (3) in the second step. If we now insert values expected in ITER ($P_{\mathrm{div}} \approx 70$ MW, $R_t \approx 6$ m, $\frac{B_\phi^u}{B_\theta^u} \approx 3$, $\alpha \approx 2°$) and a value of $\lambda_q \approx 1$ mm based on recent cross-machine studies [32], we obtain from equation (5) a value of $q_{\perp,\mathrm{peak}}^t$ of approximately 200 MW m^{-2}, well above engineering limits.

To account now for a peak target heat flux reduction due to cross-field transport in the divertor, it is useful to define an integral heat flux width as follows [33]

$$\lambda_{\mathrm{int}} = \frac{\int q_\perp^t(s) 2\pi R(s) \mathrm{d}s}{2\pi R_t q_{\perp,\mathrm{peak}}^t} \cdot \frac{\sin\beta}{f_x}. \tag{6}$$

Here, s is the distance along the divertor plate and $q_{\perp,\mathrm{peak}}^t$ the maximum target heat flux, which does now not necessarily occur at the strikepoint. This definition of λ_{int} agrees with that in [33], except for the factor $\sin\beta$, which is introduced here to account for the possibility of wall tilt. In the absence of volumetric power losses, the integral on the right of equation (6) equals P_{div}. In this case, equation (6) is equivalent to equation (4) if λ_q is replaced by λ_{int}. In a wide range of experimental conditions, the quantity $q_\perp^t(s)$ is well described

by a one-sided, exponentially decaying function convoluted with a Gaussian of width S, which accounts for diffusive-like transport in the divertor volume [34]. In this case, one can write $\lambda_{\rm int} \approx \lambda_q + 1.64S$ ([35]). With typical experimental values of $S \approx \lambda_q$ in attached conditions, the peak heat flux for ITER estimated above is then reduced by a factor of 2–3. Alternative divertor geometries have the potential to increase cross-field transport and hence $\lambda_{\rm int}$, e.g. due to instabilities driven in extended low B_θ regions [36] or due to strike-point splitting [24, 37, 38]. Even then, the above estimates for ITER-like parameters and the requirement of low electron temperatures at the target to address erosion issues highlight the need for volumetric power losses and divertor detachment.

We therefore turn now to the discussion of parallel temperature gradients in the SOL, volumetric power losses, and access to detachment, and how divertor geometry might affect these aspects. Some insights can be obtained from the two-point model [8, 39]. Assuming attached conditions (constant total pressure along the magnetic field in the SOL), parallel heat flux dominated by electron heat conduction, and no volumetric losses, significant parallel temperature gradients can occur for SOL collisionalities $\nu^*_{\rm SOL} = L_\parallel/\lambda_{ee} \gtrsim 15$ ([39]), where $L_\parallel$ is the magnetic field line length from the upstream midplane to the divertor plate and $\lambda_{ee} \approx 10^{16} \times (T_e({\rm eV}))^2/n({\rm m}^{-3})$ is the electron self-collisionality length evaluated for upstream plasma parameters. Extending the two-point model to include the variations of the major radius along the divertor leg [20, 40] and radiation losses, the electron temperature and density at the divertor plate, T^t_e and n^t_e, are found to have the following dependencies

$$T^t_e \propto \frac{(q^u_\parallel)^{10/7} \cdot (1-f_{\rm rad})^2}{n^2_u L^{4/7}_\parallel} \frac{R^2_u}{R^2_t}. \tag{7}$$

$$n^t_e \propto \frac{n^3_u L^{6/7}_\parallel}{(q^u_\parallel)^{8/7} \cdot (1-f_{\rm rad})^2} \frac{R^2_t}{R^2_u}. \tag{8}$$

This suggests that low electron temperatures and hence access to detachment can be achieved by decreasing the upstream parallel heat flux ($q^u_\parallel$) or increasing the upstream density n_u. According to equation (7), T^t_e can also be reduced by geometrical means by increasing $L_\parallel$ and, with a much stronger dependence, by increasing R_t (note that some weaker dependencies on R_u/R_t have been omitted in equation (7), [20]).

The target electron temperature can also be efficiently reduced by volumetric power losses, represented in equation (7) by the fraction $f_{\rm rad}$ of the parallel heat flux that is lost by radiation. The exact dependence of T^t_e on $f_{\rm rad}$ depends on the location along the magnetic field where the radiation occurs. In equation (7), we have assumed it occurred close to the divertor plates. It is expected that $f_{\rm rad}$ also depends on divertor geometry, primarily on divertor volume and connection length, providing a larger volume and a larger distance to convert particle energy into radiation. It is therefore useful to review the relation between flux expansion, divertor volume, and connection length. We consider the small test volume bounded by two flux surfaces and with a poloidal length Δz, as shown in figure 1(c). Introducing the local flux expansion $f_{x,\rm loc}$, representing the ratio of the flux surface spacing between the location of the test volume and the upstream midplane, we can write:

$$\Delta V = 2\pi \Delta r^u \Delta z \cdot R \cdot f_{x,\rm loc} \tag{9}$$

$$\Delta L_\parallel = \frac{B}{B_\phi}\frac{B^u_\phi}{B^u_\theta}\Delta z \cdot f_{x,\rm loc} \approx \frac{B^u_\phi}{B^u_\theta}\Delta z \cdot f_{x,\rm loc}. \tag{10}$$

Equations (9) and (10) in particular show that divertor volume and connection length are closely linked, with $\Delta V \propto R \cdot \Delta L_\parallel$ for fixed upstream parameters.

While equation (7) highlights how divertor geometry might influence access to detachment, divertor geometry is also expected to influence the behaviour in detached conditions. In particular, it has been proposed that poloidal flux expansion [31], and in particular flux flaring near the target [30], improves detachment stability, that is, it reduces the sensitivity of the location of the cold radiating region along the divertor leg on control parameters such as upstream density, power, or impurity levels. Improved radiation location stability is expected to be even more pronounced if R is varied [29–31]. This is mainly related to the dependence of $q_\parallel \propto B$ and $B \approx B_\phi \propto 1/R$. Other effects, such as changes in cross-field transport and neutral dynamics, are also expected to be important. For example, recent SXD simulations highlight the role of neutral baffling and high divertor neutral densities in the detachment process [23].

Clearly, many of the alternative divertor geometries will come at additional cost, e.g. due to a larger divertor volume, the need for additional poloidal field coils, and/or new concepts for efficient neutral baffling. These aspects will of course also have to be included in an assessment of the advantages and drawbacks of the various geometries.

In the discussion so far, we have focused on the outer divertor leg. The reason is that in the normal field direction (ion ∇B drift towards the primary X-point), the inner divertor leg often detaches more easily [41]. Furthermore, there is of course the option to run a reactor in up–down symmetric double-null configuration, where most of the exhaust heat is channeled through the outer divertor legs below and above the plasma. Nevertheless, the arguments above also apply to the inner divertor leg. In addition to wall tilt and poloidal flux expansion, even total flux expansion can in principle be achieved for the inner leg in so-called double-decker geometries [42].

An aspect which we do not discuss here is that the inner and outer divertor legs are not necessarily independent. For example, ExB drifts between the two legs, in the private flux region, can cause substantial in–out asymmetries [43].

3. Experimental approach and key diagnostics

The experiments are performed at the TCV tokamak at EPFL, a medium sized tokamak ($R_0 \approx 0.88$ m, $B_0 \approx 1.44$ T) with unique shaping capabilities due to 16 independently controllable poloidal field coils and an open vessel structure [44–46].

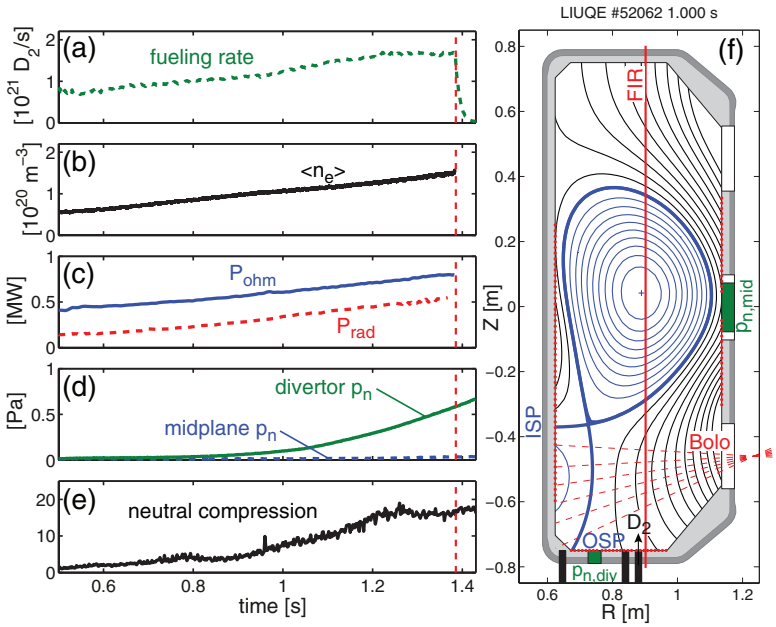

Figure 2. (*a*)–(*e*) Typical time histories of some basic parameters during the Ohmic density ramp experiments performed in this work. The vertical, dashed line indicates the time when the discharge disrupts. (*f*) Corresponding magnetic equilibrium. Highlighted are the radial locations of the three available gas valves (black rectangles), the ports onto which the pressure gauges are attached via extension tubes (green rectangles), and the locations of the 114 wall LPs (red dots). The vertical line represents the far infrared interferometer chord used to determine the line-averaged density and the dashed lines indicate divertor bolometer chords. ISP and OSP stand for inner and outer strikepoint.

We explore detachment in the various divertor geometries using Ohmic density ramps. To access high densities favourable for detachment, we run with a relatively high plasma current of $\approx$ 340 kA, resulting in $q_{95} \approx 2.45$. As in most previous detachment studies on TCV [47–51], we operate with the ion ∇B drift away from the primary X-point, which should facilitate access to the detachment of the OSP and avoid transitions to the H-mode.

Some basic characteristics of such a density ramp experiment are illustrated in figure 2 along with the magnetic geometry and the TCV vessel structure. The discharge is fuelled by injecting deuterium gas from the outermost of the three toroidally localized gas valves on the floor of the machine. These valves consist of a piezo-electric crystal with integrated flow measurement [52, 53], providing calibrated, instantaneous flow rates. The fuelling rate shown in figure 2(*a*) is feedback controlled to achieve an approximately linearly increasing line-averaged density up to the disruption (see figure 2(*b*)). The Ohmic heating power also increases throughout the density ramp due to an increase in the plasma resistivity, as is shown in figure 2(*c*) along with the total radiated power determined from foil bolometer arrays. Tomographically inverted bolometer measurements in a plasma identical to the one considered here, except for a 40% lower poloidal flux expansion at the outer target, have been employed to determine the radiated power in different plasma regions as a function of line-averaged density [50]. Radiation in the inner and outer legs was found to stop increasing approximately at the onset of detachment of the outer target, while radiation from the outer midplane SOL continued to increase and eventually became the dominant source of radiation outside the confined plasma. This seems to be related to a broadening of the upstream density profile and a resulting increase in carbon sputtering in this region [50, 54]. Clearly, the carbon concentration and its poloidal distribution is not constant during such density ramps, which constitutes a complication in the interpretation of such 'intrinsically seeded' experiments.

In figure 2(*d*), divertor and midplane neutral pressures are shown. They are obtained from recently installed, magnetically shielded and vibrationally isolated baratron pressure gauges similar to those at JET [55]. These baratrons are installed outside the toroidal field coils and are connected to the vessel by dedicated extension tubes which access the vessel through the ports highlighted in green in figure 2(*f*). Tests with and without a magnetic field in the absence of plasma have been performed to confirm proper operation of these gauges and the estimated time response of the entire system of about 70 − 100 ms was confirmed experimentally. These measurements show that divertor neutral pressure increases steadily during the density ramp, reaching values of about 0.6 Pa. The midplane pressure increases more slowly, staying below 0.04 Pa. Therefore, neutral compression shown in figure 2(*e*) increases during the discharge, reaching values of $\approx$15. It should be noted that, depending on the divertor geometry, the port connected to the divertor gauge is located in the private flux region near the strike point, as in the present case, or further out in the common flux region. When the divertor gauge measures the private flux region pressure, values lower by a factor of 2–3 than those in figure 2(*d*) are obtained under similar conditions.

In figures 3 and 4, we present some key features of the detachment behaviour of the outer leg for the discharge of

figure 2. In parallel, we introduce the diagnostics used in the subsequent sections to compare detachment behaviour in the different alternative divertor geometries. For additional recent insight on detachment in similar conditions, we refer the reader to [50, 51].

Of importance in the following are the measurements from the wall Langmuir probes [56] (LPs). The locations of the currently 114 LPs installed in TCV are indicated by red dots in figure 2(*f*). The cylindrical tips have a diameter of 4 mm. They are embedded flush into the tiles except on the floor, where they have a dome-shaped head, protruding from the tile shadow by 1 mm. These floor probes are toroidally separated from the operated gas valve by approximately 97°. In figure 3(*a*), blue curve, we show the spatially integrated, total ion flux to the outer target obtained from the floor LPs as a function of line-averaged density. Initially, this flux increases approximately linearly with line-averaged density $\langle n_e \rangle$. Then, at a density of $\langle n_e \rangle \approx 10^{20}\,\mathrm{m}^{-3}$, a clear roll-over, characteristic for the onset of detachment, occurs. Following [41], we can determine an integral degree of detachment (DoD). From the two-point model [39, 41] in the high-recycling regime, the ion flux density Γ_i is expected to be proportional to $\langle n_e \rangle^2$ if we assume $n_u \propto \langle n_e \rangle$ and neglect weaker dependences (from equations (7) and (8), we expect Γ_i to scale as $\Gamma_i \propto n_e^t \sqrt{T_e^t} \propto (R_t/R_u) \cdot L_\parallel^{4/7} \cdot (q_\parallel^u)^{-3/7} \cdot (1 - f_{\mathrm{rad}})^{-1} \cdot n_u^2$). The DoD is then defined as the ratio of the target ion flux expected from the two-point model and the actually measured one, being $\gg 1$ for a detached divertor. DoDs for the integral and peak target ion flux are defined analogously [41]. In figure 3(*b*), the integral DoD is shown for the outer target (blue curve). It reaches values of ≈10, while the peak DoD, not shown, is about twice as high. These values are consistent with previous studies on TCV in similar conditions [47] and comparable to those in L-mode density ramp experiments on JET with a carbon wall and in forward field [57]. It should be noted that since the outer target ion flux does not increase here with the square of $\langle n_e \rangle$ in attached conditions, the definition of the DoD depends on the density for which we force DoD = 1. In the present case, this is done for the lowest densities (figure 3(*a*)). If the DoD was instead set to 1 right before the roll-over, its value would be approximately 30% lower.

In contrast to the behaviour at the outer target, the total ion flux to the inner target, also shown in figure 3(*a*), shows no clear roll-over and, consequently, the integral DoD in figure 3(*b*) remains low. This is typical for these 'unfavourable' ion ∇B drift plasmas, where the inner strike point typically stays attached at TCV [47–50].

In figures 3(*c*) and (*d*), we present radial profiles of ion saturation current and parallel heat flux measured along the outer strikepoint during the low and high density phases highlighted in figure 3(*a*). As the radial coordinate, we use $\rho_\psi = \sqrt{(\psi - \psi_0)/(\psi_{x1} - \psi_0)}$, where ψ is the poloidal flux and ψ_0 and ψ_{x1} its value at the magnetic axis and at the primary X-point, respectively. To directly relate ρ_ψ to real space coordinates, its values, corresponding to an upstream radial distance from the separatrix of 0 mm, 5 mm, and 10 mm, are represented by vertical lines. Figure 3(*c*) reveals a clear reduction

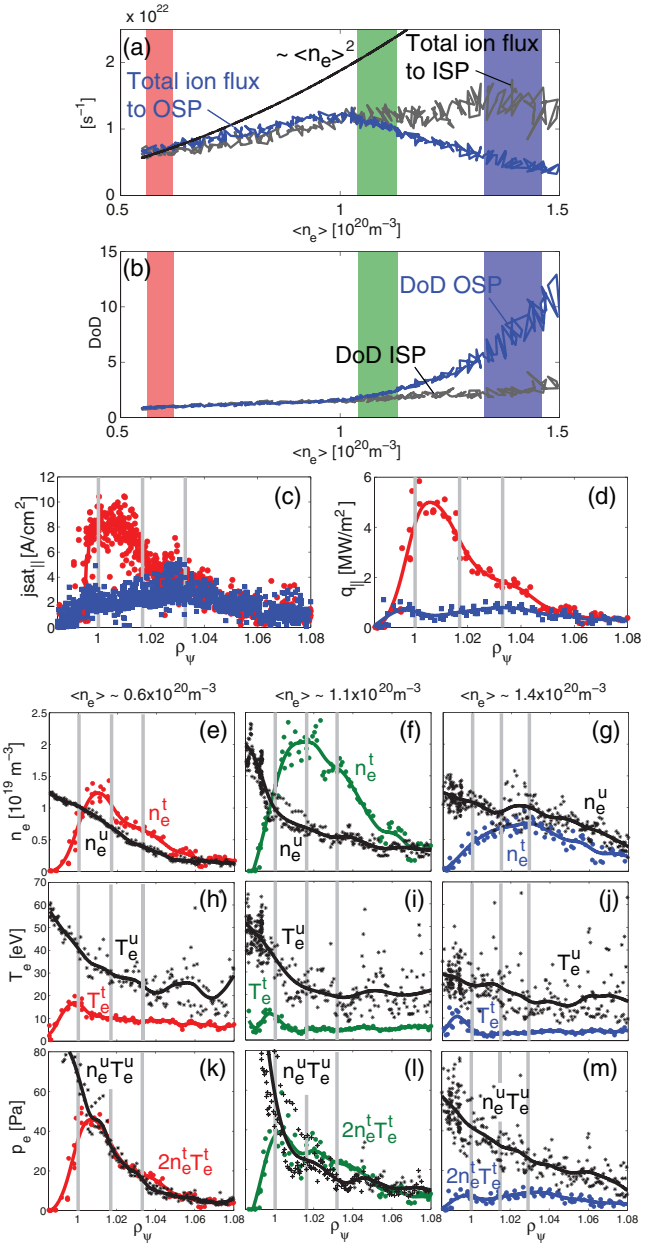

Figure 3. Key measurements from the wall LPs and the midplane fast reciprocating probe for the discharge in figure 2. (*a*)–(*b*) Total ion flux and integral DoD at the outer (blue) and inner (grey) target versus line-averaged density. (*c*)–(*d*) Ion saturation current and parallel heat flux profiles at the outer target at the lowest and highest densities highlighted in (*a*) and (*b*) by the shaded regions. (*e*)–(*m*) Comparison of density, temperature, and pressure profiles at the upstream midplane and the target for different densities. The left column corresponds to the lowest, the middle column to the intermediate, and the right column to the highest density ranges highlighted in (*a*) and (*b*). The vertical, grey lines indicate the ρ_ψ values corresponding to a midplane separatrix distance of 0 mm, 5 mm, and 10 mm.

in particle flux in the vicinity of the separatrix, up to a factor of approximately 4, and negligible changes at $\rho_\psi \geqslant 1.04$. Figure 3(*d*) reveals a substantial reduction of the parallel heat flux, up to a factor ≈10, across most of the profile. These parallel heat fluxes to the outer strikepoint are determined from [39]

$$q_{\parallel}^{t} = e n_e^t c_s (\gamma T_e^t + E_{\rm pot}), \tag{11}$$

where $c_s = \sqrt{(T_e^t + T_i^t)/m_i}$ is the ion sound speed (for which we assume $T_i^t = T_e^t$), $E_{\rm pot} = 13.6 + 2.2$ eV is the potential energy carried by each outgoing ion, including the hydrogen ionization energy and half of the molecular binding energy, and γ is the sheath heat transmission factor, taken to be $\gamma = 5$ (see also [19, 58]). The wall LPs are operated in a triangular voltage sweep (-120 to $+80$ V, frequency $= 330$ Hz). The quantities n_e^t and T_e^t are then determined from the time-averaged I– V characteristics (averaged over 50 ms) as described in [59], a procedure which has been validated against triple probe measurements [60].

In figures 3(*e*)–(*m*), we compare density, electron temperature, and total electron pressure, measured at the outboard midplane with a fast reciprocating probe and at the target with the wall LPs. Profiles corresponding to the three different density ranges highlighted in figure 3(*a*) are shown. We see that at the lowest densities, a clear temperature gradient along the magnetic field already exists (figure 3(*h*)). At the same time, upstream and target pressure agree well up to the separatrix, (*k*), indicating a high-recycling regime. Just after the roll-over in the ion flux, density at the target has increased, (*f*), while upstream and target pressure still approximately match, (*l*). At maximum line-averaged density, finally, a clear pressure gradient along the field has been established, (*m*), associated with a reduction in target density and temperature, (*g*) and (*j*). It should be noted that the radial alignment between upstream and target profiles is subject to uncertainties in the magnetic reconstruction. Therefore, while figures 3(*e*)–(*m*) show a robust trend in the development of parallel pressure gradients with increasing density, the excellent pressure balance at low density for instance might be a bit fortuitous. Also noteworthy are the relatively high values of target electron temperature, reaching values $\gtrsim 10$ eV, for $\rho_\psi < 1$ even at the highest core densities in figure 3(*j*). These measurements are suspicious, given that for these probes, the difference between the floating potential and the plasma potential (determined as the probe potential where the electron current starts to saturate) is much smaller than $\approx$3.5 times the evaluated electron temperature, as would be expected from sheath physics [39]. Different fitting techniques are currently being tested to explore this issue.

In order to also gain information on the detachment behaviour in the region between the target and X-point, we use measurements from the Multicam diagnostic. This system images the plasma in the divertor with a tangential view at 40 Hz. It provides line-integrated, two-dimensional measurements of up to four individual emission lines simultaneously from the same optics using beam splitters and appropriate filters. The measurement location of the Multicam is separated toroidally from the operated gas valve by approximately 150°. Here, we focus on CIII (465 nm) line emission and determine the uncalibrated emissivity profiles from tomographic inversion [50]. Example frames at different times during the density ramp are shown in figure 4. Focusing on the emissivity along the outer leg, it is apparent that, initially, the emissivity is concentrated near the strikepoint (figure 4(*a*)). Later in time, as the core plasma density increases and the leg cools down (figures 4(*b*) and (*c*)) the lower edge of the emissivity region moves upstream towards the X-point. At the relevant densities, such a drop in CIII emissivity is expected at an electron temperature of about 3–8 eV [50, 61, 62]. Preliminary LP measurements on TCV for a discharge very similar to the one discussed here, which does not feature the private flux region T_e peak in figures 3(*i*)–(*j*), indicates a temperature closer to the higher limit. Further direct experimental investigations of this will be the subject of studies in the near future. In the following, we will use the CIII front as a proxy for the location of the cold, radiative region. We determine this location as the position where the CIII emissivity along the outer leg has dropped to half its peak value. We then evaluate the poloidal distance of this CIII edge along the outer leg between the strikepoint and X-point as a function of line-averaged density. The result of this analysis is displayed in figure 4(*d*). Comparison with figure 3(*a*) shows that the CIII radiation starts to detach from the target at a line-averaged density about 10%–15% lower than the roll-over density of the outer target ion flux.

The upstream movement of the CIII emission edge is actually similar to the movement of the total radiation peak, also shown in figure 4(*d*). It is obtained by detecting the times at which the radiation measured along the divertor bolometer chords in figure 2(*f*) attains its maximum. This observation provides further motivation for using the spatially better resolved CIII emission edge as the location of the radiation region.

The measurements presented in this section show key characteristics of detachment, such as reductions of target particle and heat fluxes, a cooling of the plasma in the divertor leg, and the development of parallel pressure gradients. At the same time, there are characteristics of TCV divertor plasmas which differ from the general detachment picture. In particular, contrary to higher density tokamaks, volumetric recombination and density remain peaked near the strikepoint throughout the density ramp [51], as opposed to rapidly moving to the primary X-point as detachment evolves.

In the following, when we compare detachment behaviour in the different geometries, we mainly focus on the evolution of the integrated ion flux (figure 3(*a*)) and the movement of the CIII front (figure 4(*d*)). The roll-over of the ion flux and the start of the CIII front movement are taken as measures of the detachment threshold, the extent of the roll-over in ion flux is used as an indication of the level of detachment, and the density window between the start of the CIII front movement and when it arrives at the X-point is taken as a measure of the radiation location sensitivity. As the understanding of detachment on TCV evolves, these criteria might also be refined in the future.

4. Poloidal flux expansion scan; XDs

Detachment in Ohmic density ramps, as discussed in the previous section, is explored here in configurations with varying poloidal flux expansion, as shown in figure 5 (the configuration discussed in section 3 is identical to that in figure 5(*c*)). These equilibria also feature poloidal flux flaring, i.e. an increase of $f_{x,\rm loc}$ towards the target, characteristic for the XD

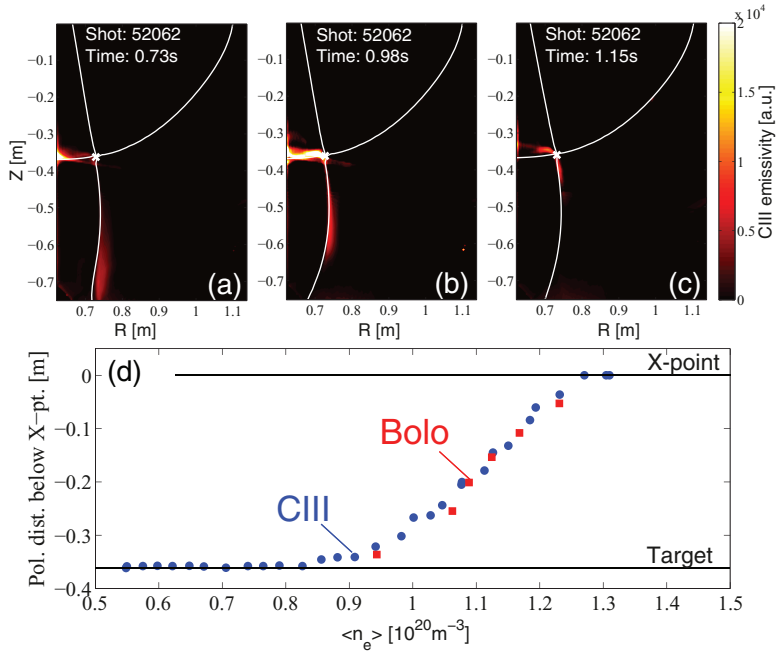

Figure 4. (*a*)–(*c*) Uncalibrated CIII (465 nm) emissivity profiles across the divertor volume for different time periods during the density ramp experiment in figure 2. (*d*) Position of the CIII radiation front along the outer leg as a function of line-averaged density together with the total radiation peak position determined from the divertor bolometer views indicated in figure 2(*f*).

[27]. These configurations are similar to those used in the pioneering detachment studies at TCV in [47]. The main difference here is a vertical shift of the plasma position to make these plasmas compatible with the recently installed neutral beam heating system [63] for future, higher power detachment studies.

The different equilibria in figure 5 are labelled by the value of f_x at an upstream radial distance from the separatrix of 6 mm, corresponding to about one λ_q on TCV [64]. The actual radial profiles of f_x are shown in figure 5(*e*). Across the different geometries, this quantity varies by about a factor of 10. According to equation (10), an increase in f_x results in an increase in connection length, which we take here as the magnetic field line length between the midplane and the outer target. Between the $f_x = 2.0$ and the $f_x = 21$ case, this amounts to about a two-fold increase in $L_\parallel$, as is apparent from figure 5(*f*). At the same time, the incidence angle of the magnetic field on the floor is reduced with increasing f_x from $\approx 6°$ to close to $\approx 0°$, as shown in figure 5(*g*).

In figure 6(*a*), we plot the total ion flux to the OSP as a function of line-averaged density for the different geometries. At low density, the total flux depends relatively weakly on f_x, except for the $f_x = 21$ case, for which substantially smaller fluxes are measured throughout the density ramp. As the density is increased, a roll-over in the flux is observed. It becomes more and more pronounced the larger f_x is, although the most significant change occurs between the $f_x = 2.0$ and the $f_x = 5.0$ cases, and changes are relatively small for $f_x \geqslant 5$. This more pronounced roll-over indicates that a deeper detachment is achieved for larger f_x at a given line-averaged density. To be more quantitative, we evaluate the degree of detachment for the different cases as in figures 3(*a*)–(*b*). For $\langle n_e \rangle = 1.4 \cdot 10^{20}$ m^{-3}, we then find the following values of the integral DoDs: 3 ($f_x = 2$), 4.8 ($f_x = 5$), 5.9 ($f_x = 7.4$), 7.7 ($f_x = 10$), and 8.3 ($f_x = 21$).

From equation (7), we would expect a reduction in the threshold density for detachment with increasing $L_\parallel$, either directly through the $L_\parallel^{4/7}$ dependence or through a potential $L_\parallel$-dependence of $f_{\rm rad}$. For the doubling of $L_\parallel$ between the most extreme cases in figure 5, a relatively weak reduction of n_u by a factor $1/(2^{2/7}) \approx 0.82$ is sufficient to compensate the $L_\parallel$ increase in the denominator of equation (7). The experimental data in figure 6(*a*) does not reveal a significant trend in roll-over density, at least for the cases with $f_x \geqslant 5$ where the roll-over density is well defined.

If we instead consider the peak parallel ion flux to the OSP, shown in figure 6(*b*), the trend is even opposite to what is expected based on equation (7). The peak flux drops slightly earlier for lower f_x cases (please note that the strong variation in the $f_x = 2.0$ data is due to strike-point sweeps, which have been performed due to the otherwise insufficient spatial resolution of the wall LPs in this case). This observation is consistent with previous experiments in similar configurations [47]. Contrary to the integral DoD, the peak DoD does not show a clear trend across the different configurations and lies in the range 12–15 for all cases and $\langle n_e \rangle = 1.4 \cdot 10^{20}$ m^{-3}.

To gain further insight, it is instructive to look at the ion saturation current profiles, which are shown in figures 6(*c*)–(*f*) for the $f_x = 2.0$, $f_x = 10$, and $f_x = 21$ cases and different line-averaged densities. Clearly, the ion saturation current density perpendicular to the floor strongly varies with f_x. In order to remove these geometrical effects, figures 6(*c*)–(*f*) show the ion saturation current parallel to the field as a function of ρ_ψ. It is apparent that even at the lowest densities considered here, the $j_{{\rm sat}\parallel}$ profiles differ in flux space between the different

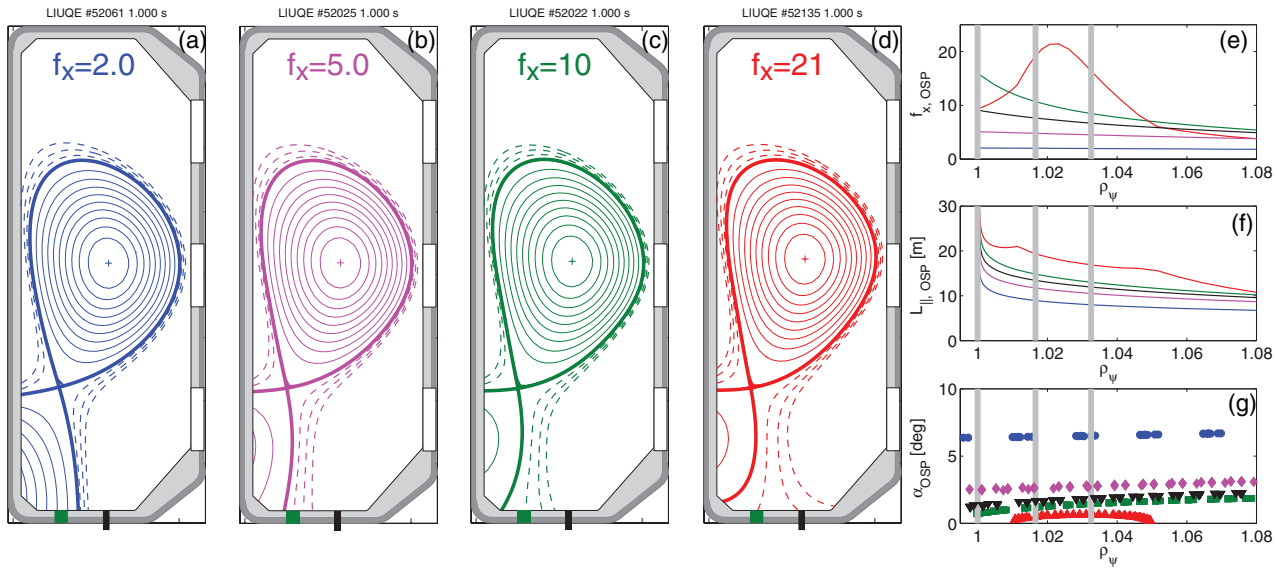

Figure 5. Geometrical properties of the discharges with different levels of poloidal flux expansion. (*a*)–(*d*) show the different magnetic equilibria. The black rectangle on the floor indicates the fulling valve location, the green one indicates the location of the neutral pressure measurement. (*e*)–(*g*) show, for the outer strikepoint, radial profiles of poloidal flux expansion, connection length, and magnetic field line incidence angles at the target. The colours correspond to the equilibria in (*a*)–(*d*) (the equilibrium of the intermediate, black case is not shown). The vertical, grey lines indicate the ρ_ψ values corresponding to a midplane separatrix distance of 0 mm, 5 mm, and 10 mm.

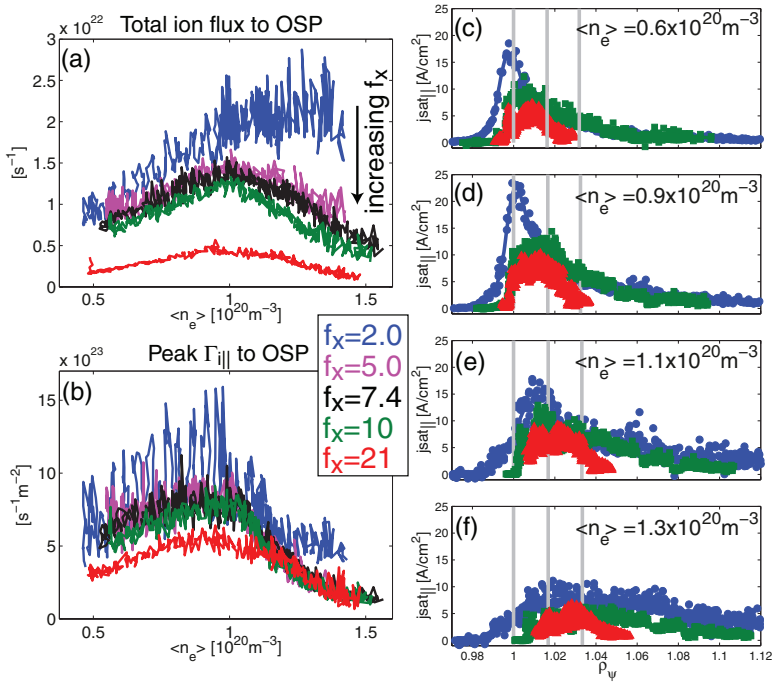

Figure 6. Behaviour of the ion flux to the outer target as a function of line-averaged density for the different values of poloidal flux expansion in figure 5 (please note that the equilibrium for the $f_x = 7.4$ case has been omitted in figure 5). (*a*) shows the integrated, total ion flux to the outer target, (*b*) shows the peak parallel ion flux, and (*c*)–(*f*) show ion saturation current profiles at different densities and for the $f_x = 2.0$, $f_x = 10$, and $f_x = 21$ cases.

geometries. In particular, the profile for the $f_x = 2.0$ case is more peaked with steeper gradients, which translates into even steeper gradients in actual, real space coordinates than would be expected from geometry alone. This strong peaking points to profile effects, which could be the reason for the different relative evolution of total and peak ion flux between the different geometries.

Figures 6(*c*)–(*f*) also indicate why the total measured particle flux is so much weaker in the extreme XD, the $f_x = 21$ case. First, poloidal flux expansion is so large in this case that only part of the strikepoint is covered by the probes, resulting in a $j_{\mathrm{sat}\parallel}$ profile that is limited in ρ_ψ. Second, a rather steep decrease is observed in the $j_{\mathrm{sat}\parallel}$ profiles for $\rho_\psi \gtrsim 1.04$. This is the region where the incidence angle of the magnetic field on

the floor drops to 0° (see figure 5(*g*)). Even though the floor probes protrude by 1 mm from the floor, they might measure a reduced flux due to toroidal shadowing at these small angles. Besides being challenging to diagnose, the toroidal asymmetries and local hot spots which can occur in geometries with very small target angles constitute a serious limitation of these geometries, at least in attached conditions. In a deeply detached divertor, this issue is, however, expected to be much less severe [65].

In figure 7, we compare the dependence of the CIII front location on the line-averaged density for different flux expansion. For the $f_x = 2.0$ case, data from three similar discharges from two different experimental days are shown, showing good reproducibility. These curves reveal a rather strong dependence of the radiation location on density. With increasing flux expansion, this radiation location sensitivity decreases from a rate of $\approx 1.25 \cdot 10^{-20}$ m m^{-3} for the $f_x = 2.0$ case to a rate of $\approx 0.7 \cdot 10^{-20}$ m m^{-3} for the $f_x = 21$ case. This reduced sensitivity is essential for better detachment control and qualitatively confirms the predictions [30, 31]. The start of the front movement occurs at slightly lower densities than the roll-over in ion current in figure 6(*a*), and is also rather insensitive to the value of f_x.

In figure 8(*a*), filled squares, the divertor neutral pressure for the different flux expansion cases is plotted as a function of the ρ_ψ-position of the pressure gauge. These pressure values are obtained for a line-averaged density of $\langle n_e \rangle = 1.25 \cdot 10^{20}$ m^{-3}, that is, well after the onset of detachment. For the $f_x = 2.0$ case, the pressure gauge is located in the private flux region, while for the cases $f_x = 5 - 21$, the gauge is located in the common flux region near the strike-point, in the range $\rho_\psi = 1.01 - 1.025$ indicated by the shaded region. For the latter cases, we observe a monotonic decrease of p_n with flux expansion. Interestingly, plotting the neutral pressure for these cases as a function of the sine of the magnetic field line incidence angle α reveals a fairly linear trend (figure 8(*b*)). This suggests that the neutral pressure measured at this location is proportional to the ion flux perpendicular to the floor. Extrapolating this linear trend for the $f_x = 2.0$ case results in $p_n \approx 1.1$ Pa.

Unfortunately, no neutral pressure measurements are available in the private flux region for the $f_x = 5 - 21$ cases, so we cannot comment on the differences in the neutral pressures in this region.

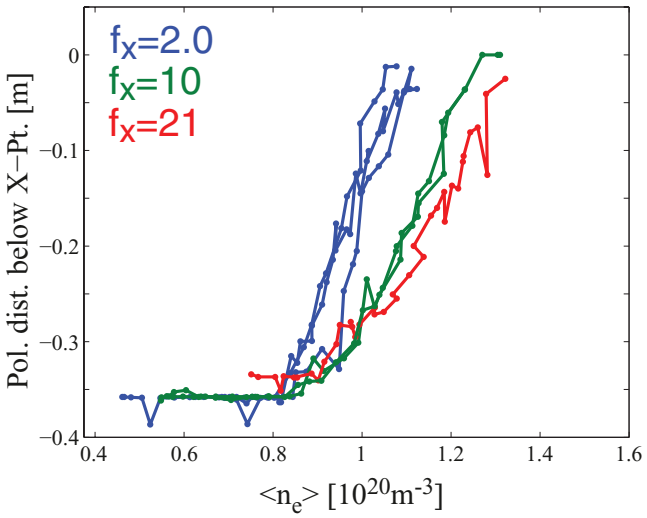

Figure 7. Dependence of the CIII emission front location between the OSP and the X-point on line-averaged density for three values of poloidal flux expansion. For the $f_x = 2.0$ ($f_x = 10$) case, data from 3 (2) similar discharges is shown.

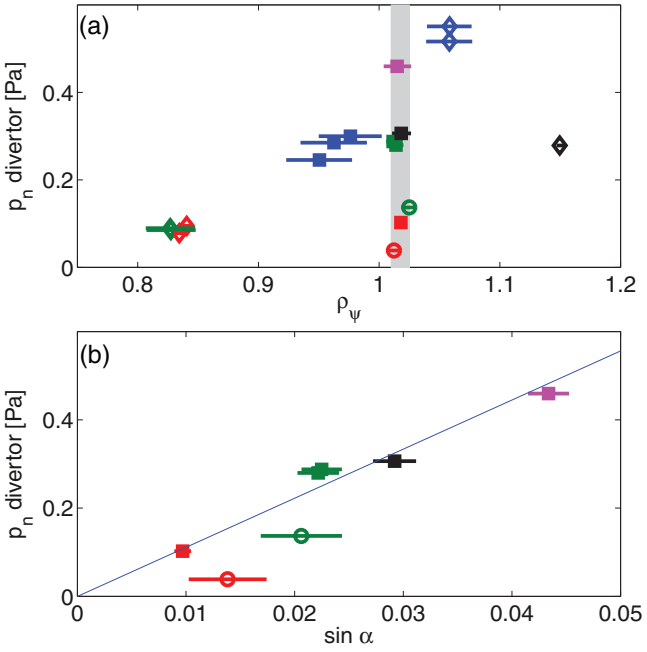

Figure 8. Neutral pressures measured with the divertor gauge for a line-averaged density of $\langle n_e \rangle = 1.25 \cdot 10^{20}$ m^{-3} and the geometries shown in figure 5 (filled squares), figure 9 (diamonds), and figure 13 (circles). In (*a*), p_n is shown as a function of the ρ_ψ position of the gauge. (*b*) shows the pressure for the cases where $1.01 < \rho_\psi < 1.025$ as a function of the sine of the magnetic field line incidence angle on the floor.

5. Total flux expansion scan; SXDs

We now turn to a set of experiments where the major radius of the OSP is varied in order to explore the effect of total flux expansion. As apparent in figure 9, R_t is varied from $R_t \approx 0.62$ m to $R_t \approx 1.06$ m. Care was taken to keep other quantities as constant as possible, in particular connection length and flux expansion, which is fairly well achieved, as is shown in figures 9(*e*)–(*f*). Unfortunately, the OSP is only covered by the LPs for the two intermediate R_t-cases, and we therefore first focus on them. The plots equivalent to figure 6 for these two cases are shown in figure 10. They reveal a similar behaviour of the ion flux in the two cases. In particular, there is no indication that the larger R_t case detaches earlier, as we would have expected from the R_t dependence in equation (7). The CIII front movement for the two cases in figure 11(*a*) suggests even a slightly lower detachment threshold for the smaller R_t case. Furthermore, this data also shows no indication for a decrease in radiation location sensitivity at larger R_t. The CIII analysis can also be performed for the extreme R_t cases

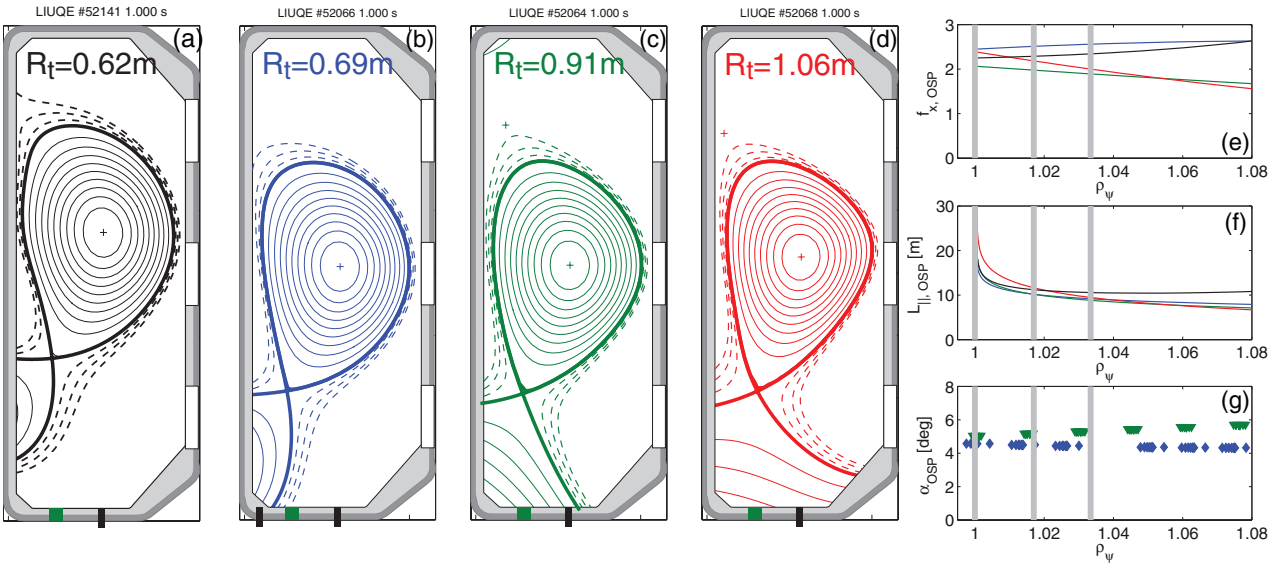

Figure 9. The equivalent to figure 5, showing geometrical properties of the discharges with different outer strikepoint major radii.

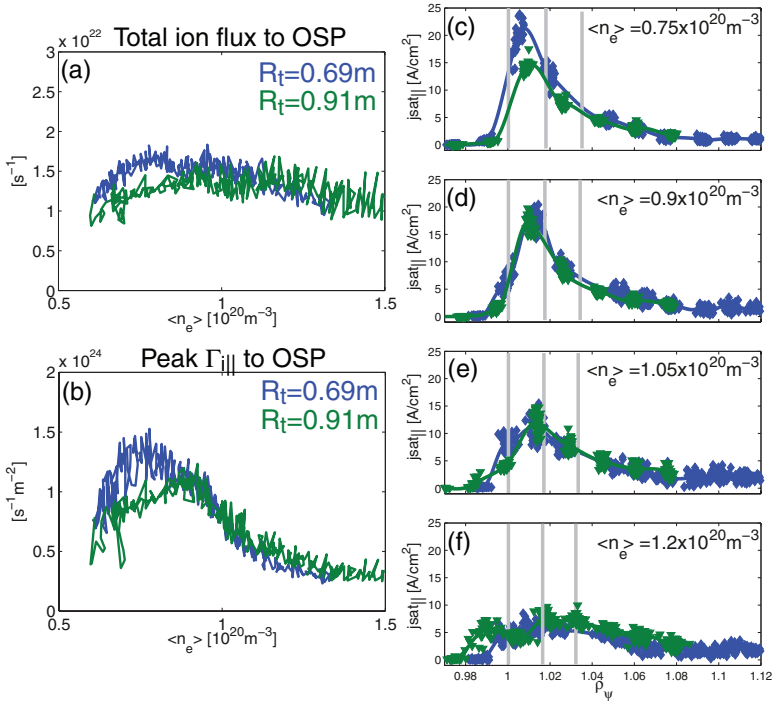

Figure 10. Behaviour of the ion flux to the outer target for the two intermediate R_t cases in figure 9, for which the outer strikepoint is covered by LPs. As in figure 6, the integrated (*a*) and the peak parallel (*b*) ion fluxes are shown, as well as the radial profiles of $j_{\mathrm{sat},\parallel}$ at different densities, (*c*)–(*f*).

and the result is shown in figure 11(*b*). This reveals a similar behaviour for the $R_t \approx 0.62$ m and $R_t \approx 1.06$ m cases. Again, there is no indication of a reduced detachment threshold or a decrease in radiation location sensitivity with increasing R_t.

In section 4, we observed a rather strong dependence of detachment behaviour on flux expansion, especially at low values of f_x. This raises the question as to whether the somewhat smaller f_x values for the larger R_t cases, figure 9(*e*), might mask any R_t dependence. To explore this point, discharges with $R_t = 1.06$ m have been performed where f_x was increased in the near SOL by about 50% compared to the equilibrium in figure 9 (d). The value of f_x was then above that of the $R_t = 0.62$ m case up to $\rho_\psi \approx 1.05$. The result was that the CIII front movement was not significantly affected by this change in f_x (not shown).

Another potential difference between, e.g. the $R_t = 0.69$ m and $R_t = 0.91$ m cases is the fuelling location. The outermost valve in figure 2(*f*) is used in both cases, which results in main chamber fuelling for the $R_t = 0.69$ m case and private flux region fuelling for the $R_t = 0.91$ m case (the valve locations are also highlighted in figures 9(*b*) and (*c*)). A test with fuelling from the innermost valve for the $R_t = 0.69$ m

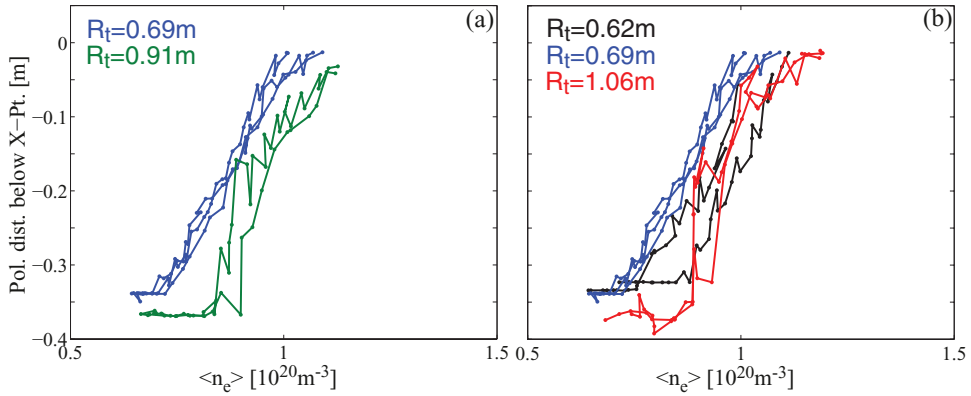

Figure 11. (*a*) Comparison of the CIII front location versus line-averaged density for the $R_t = 0.91$ m case (from two similar discharges) and the $R_t = 0.69$ m case (from three similar discharges). (*b*) Comparison of the CIII front location versus line-averaged density for the $R_t = 0.62$ m and $R_t = 1.06$ m case (from two similar discharges each) and again the $R_t = 0.69$ m case.

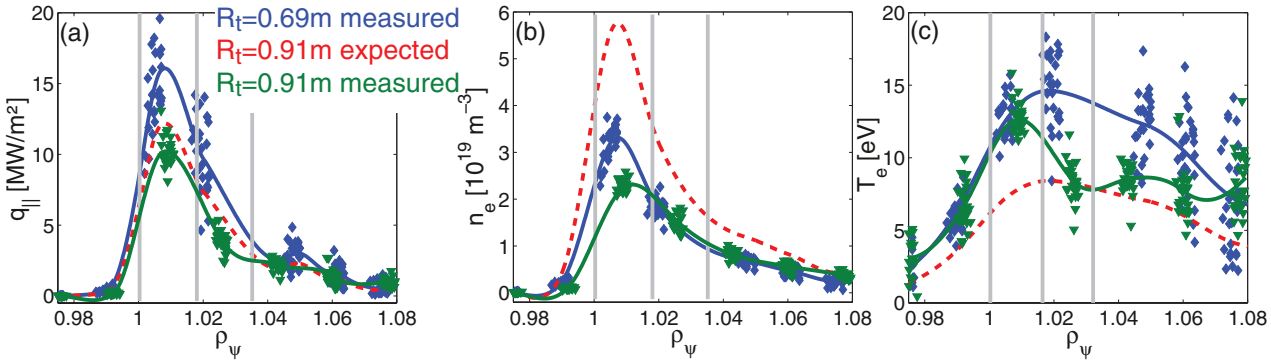

Figure 12. Comparison of the measured R_t dependence of the outer strikepoint profiles with the model predictions in attached conditions ($\langle n_e \rangle = 0.75 \cdot 10^{20}$ m^{-3}). See description in the main text.

case, however, showed no significant differences in terms of $j_{\mathrm{sat},\parallel}$ profiles, total ion flux, and CIII front movement with this change in the fuelling location.

In order to gain some insight as to why the expected benefits of increasing R_t are not observed in these experiments, we compare, in figure 12, profiles of $q^t_\parallel$, n^t_e, and T^t_e determined from the wall LPs in attached conditions ($\langle n_e \rangle = 0.75 \cdot 10^{20}$ m^{-3}) and for both the $R_t \approx 0.69$ m and $R_t \approx 0.91$ m cases. Due to total flux expansion, we expect $q^t_\parallel$ to scale approximately as $1/R_t$. In figure 12(*a*), the dashed, red curve is the profile of $q^t_\parallel$ expected for the $R_t \approx 0.91$ m case based on the measurement at $R_t \approx 0.69$ m and the $1/R_t$ dependence. Within limited spatial resolution, the measurements are consistent with this trend. Next, we explore the two-point model predictions, which state that T^t_e scales roughly as $1/R^2_t$ and n^t_e as R^2_t (see equations (7) and (8)). Figures 12(*b*)–(*c*) show again the measurements for the $R_t \approx 0.69$ m case, the values expected from this for $R_t \approx 0.91$ m assuming the above R_t-dependencies, as well as the actual measurements for this case. Some reduction in T^t_e is indeed observed with an increase in R_t, at least across part of the profile. However, the expected increase in target density is clearly absent. While the reason for the deviation from the two-point model scaling is not understood at this point, this discrepancy might explain why the expected benefits of increasing R_t are not observed here.

The divertor neutral pressure values for this R_t scan and for $\langle n_e \rangle = 1.25 \cdot 10^{20}$ m^{-3} are shown in figure 8(*a*) (diamonds). This reveals that p_n peaks near the strikepoint and decreases both towards the common and private flux region.

6. Additional X-points near the target; XPTs

We now explore the effect of an additional X-point near the OSP. Starting from the same reference discharge as in the flux expansions scan, two XPT configurations are produced with the target X-point in the main SOL (see figure 13). Contrary to the XPT divertor proposed in [29], these configurations do not include a sizeable increase in R_t and no neutral baffling. The additional X-point results in a substantial increase, by a factor of 2–3, in $L_\parallel$, figure 13(*e*). At the radial position of the additional X-point, indicated by vertical dashed lines in figures 13(*d*)–(*f*), $L_\parallel$ diverges. Similarly as for the SF [24, 38], we label these XPT cases by the value of ρ_ψ at the additional X-point, which we indicate with ρ_{x2}. For the XPT case in figure 13(*b*), we have $\rho_{x2} \approx 1.036$ and for the case in figure 13(*c*), ρ_{x2} is ≈ 1.012.

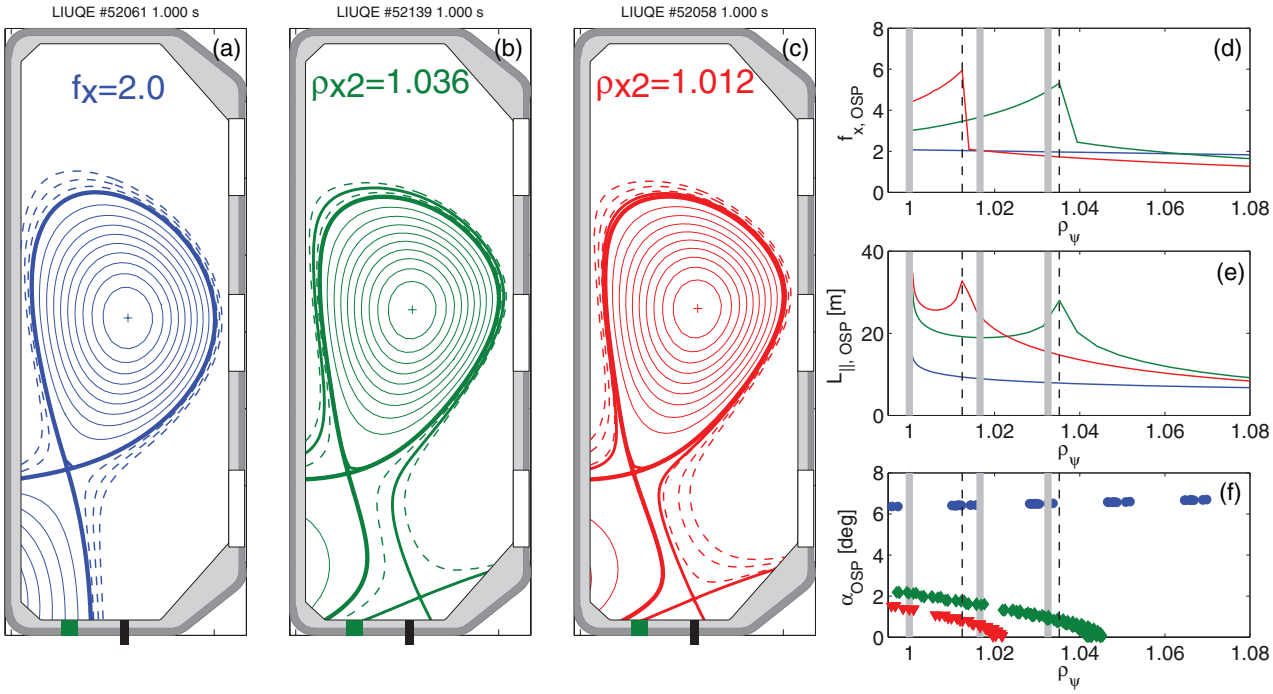

Figure 13. The equivalent to figure 5, comparing the geometrical properties of XPTs with those of a standard TCV diverted geometry with $f_x = 2.0$.

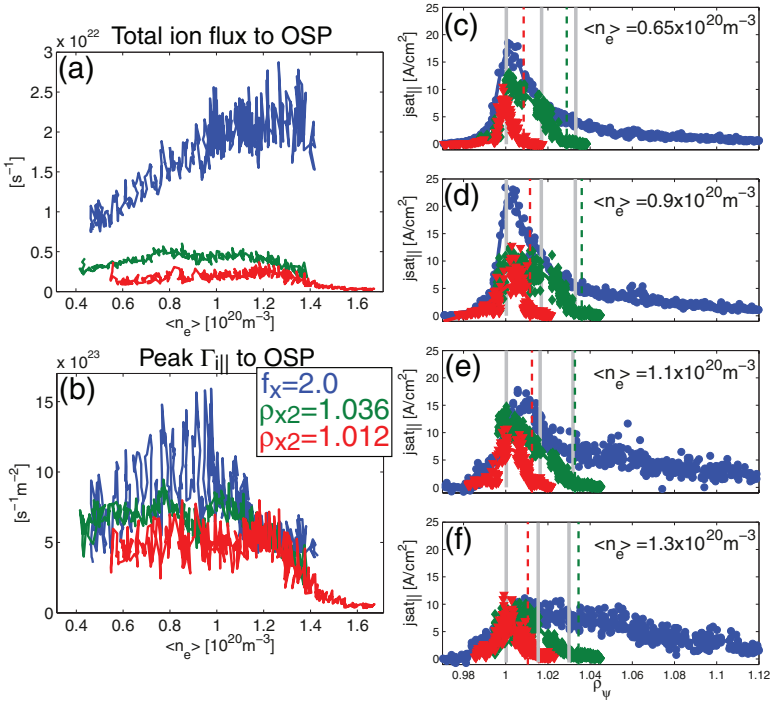

Figure 14. The equivalent to figures 6 and 10, here for comparison of the $f_x = 2.0$ case with the XPT geometries.

The additional X-point strongly reduces the incidence angle of the magnetic field on the floor compared to the reference case (figure 13(f)). The reason is a combination of reduced poloidal field and effective wall tilt. The incidence angle, however, stays above ≈0.8° for field lines in the common flux region and only approaches 0° in the private region of the target X-point.

In the XPT geometries, the SOL is split into two outer strikepoints. Unfortunately, the outer one, which sits on the inclined tile at $R \approx 1.07$ m, is currently not covered by LPs. Thus, only LP measurements from the inner part of the outer target are available. Due to this incomplete coverage, the integral ion flux shown in figure 14(a) is much lower than for the $f_x = 2.0$ case and its meaning is difficult to interpret. The

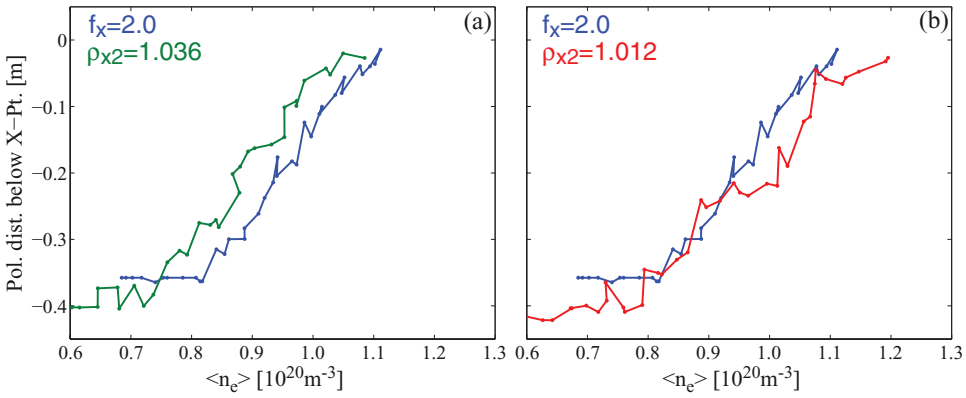

Figure 15. (*a*) Comparison of the CIII front location versus line-averaged density for the $\rho_{x2} \approx 1.036$ XPT case and the $f_x = 2.0$ case. (*b*) Comparison of the CIII front location versus line-averaged density for the $\rho_{x2} \approx 1.012$ XPT case and, again, the $f_x = 2.0$ case.

evolution of the peak ion flux in figure 14(*b*) and the individual $j_{\mathrm{sat},\parallel}$ profiles in figures 14(*c*)–(*f*), however, do not indicate any facilitated access to detachment in the XPT cases, despite the rather substantial increase in $L_\parallel$. Especially for the $\rho_{x2} \approx 1.012$ case, the peak ion flux drops even later than for the $f_x = 2.0$ case or the other f_x cases considered in section 4. It is noteworthy that the peak flux eventually drops almost to zero in the $\rho_{x2} \approx 1.012$ case. However, this occurs at densities above those achieved in the other geometries, making a comparison difficult.

We turn now to the CIII front movement in figure 15. Comparing the reference case and the $\rho_{x2} \approx 1.036$ case in figure 15(*a*), we observe a very similar front movement, aside from a shift in density. Comparison with the $\rho_{x2} \approx 1.012$ case in figure 15(*b*) is more interesting. Initially, the front movement is very similar between the two cases. Then, the front movement almost stops during a 10%–15% window in density for the XPT case, before it continues moving towards the primary X-point. This reduction in front sensitivity occurs in the vicinity of the target X-point and is an indication that the latter might allow control of the radiation location, as proposed in [29]. More experiments will be needed to quantify the importance of this effect and its dependence on ρ_{x2}.

The divertor neutral pressure measurements for the XPT cases for $\langle n_e \rangle = 1.25 \cdot 10^{20}\ \mathrm{m}^{-3}$ are shown in figure 8 (circles). The values are close to those of the extreme XD case with $f_x = 21$. They are, however, below the $\sin\alpha$ dependence identified for the poloidal flux expansion scan (see figure 8(*b*)), which could be a result of strikepoint splitting.

7. Summary and conclusions

The dependence of divertor detachment on specific aspects of the magnetic geometry is studied on TCV in Ohmic density ramp experiments with the ion ∇B drift away from the primary X-point. In a series of discharges, poloidal flux expansion f_x at the outer target is scanned by approximately a factor of 10 and the outer strikepoint major radius R_t, and hence total flux expansion, is varied by ≈70%. The effect of an additional X-point in the main SOL near the outer target is also investigated. Detachment characteristics of the outer target are assessed in these configurations based on target probe measurements and two-dimensional CIII emissivity profiles obtained from inverted camera data. As a measure of the detachment threshold, we take here the line-averaged densities where the total ion flux to the outer target exhibits a roll-over and where the CIII emissivity front starts to detach from the target. The extent of the drop in ion flux is interpreted as a measure of the level of detachment. The density window between the start of the CIII emission region's lower edge movement and when it arrives at the X-point is taken as a measure of the radiation region location sensitivity to changes in core density; lower sensitivity is essential for better control over the radiation location and detachment.

Applying this procedure to the different geometries reveals mixed agreement with the effects predicted by models: we do find that the radiation region location sensitivity to line-averaged density decreases with increasing f_x. The sensitivity of the CIII front poloidal movement on the line-averaged density is found to be even lower in the vicinity of a target X-point. However, we do not find that increasing the connection length $L_\parallel$ from the outer midplane to the target decreases the detachment threshold, despite a variation of $L_\parallel$ by factors of 2–3. Also, no systematic trend of detachment threshold and radiation location sensitivity with total flux expansion is observed.

The experiments and analysis presented here constitute a basis for more detailed studies of geometrical dependences of detachment on TCV and comparisons with modelling. Particularly puzzling at this point is the absence of a clear dependence of detachment behaviour on total flux expansion. The scaling of target density and temperature with R_t, as predicted by the two-point model, is different than that found in the experiment. This suggests the presence of additional effects. One possibility is that there are non-negligible convective contributions to the parallel heat flux, something not included in the models. In addition, the models assume that mean free paths for ionization are short and all ionization is close to the target, not found in the experiment.

An aspect which could only be addressed to a limited extent is the role of the neutrals. Their dynamics are expected to change with divertor geometry as well, which could influence the detachment behavior. The poloidal angle at the strikepoint between the separatrix and the target surface varies

substantially in the different geometries, changing from something resembling a tilted plate divertor to a horizontal plate divertor. This effective wall tilt could potentially be important. Unfortunately, the divertor gauge on TCV measures, depending on geometry, neutral pressures in different locations relative to the strikepoint, sometimes in the private flux region and sometimes in the SOL. In the present geometries, the role of the effective wall tilt on, e.g. the neutral pressure in the private flux region could not, therefore, be explored. Studying the importance of this effect requires additional pressure measurements or experiments in geometries designed specifically to explore this question.

The goal of future studies will be to complement these observations with measurements from additional diagnostics to determine the relation between divertor volume and radiated power and to perform a detailed power balance, and to extend these studies to the forward field direction and scenarios with additional heating and H-mode. This will benefit from the fact that all the geometries developed in this work are compatible with the recently installed 1MW neutral beam heating system at TCV [63].

Acknowledgment

This work has been carried out within the framework of the EUROfusion Consortium and has received funding from the Euratom research and training programme 2014–2018 under grant agreement No 633053. The views and opinions expressed herein do not necessarily reflect those of the European Commission.

References

[1] Loarte A. *et al* 2007 *Nucl. Fusion* **47** S203
[2] Zohm H. *et al* 2013 *Nucl. Fusion* **53** 073019
[3] Wischmeier M. 2015 *J. Nucl. Mater.* **463** 22–9
[4] Kallenbach A. and The ASDEX Upgrade Team 2013 *Plasma Phys. Control. Fusion* **55** 124041
[5] Dux R. and The ASDEX Upgrade Team 2009 *J. Nucl. Mater.* **390** 858–63
[6] Stangeby P.C. and Leonard A.W. 2011 *Nucl. Fusion* **51** 063001
[7] Brezinsek S. 2015 *J. Nucl. Mater.* **463** 11–21
[8] Pitcher C.S. and Stangeby P.C. 1997 *Plasma Phys. Control. Fusion* **39** 779–930
[9] Lipschultz B., LaBombard B., Terry J.L., Boswell C. and Hutchinson I.H. 2007 *Fusion Sci. Technol.* **51** 369
[10] Fenstermacher M.E. *et al* 1999 *Plasma Phys. Control. Fusion* **41** A345–55
[11] Pitts R.A., Kukushkin A., Loarte A., Martin A., Merola M., Kessel C.E., Komarov V. and Shimada M. 2009 *Phys. Scr. T* **138** 014001
[12] Fundamenski W. 2009 *J. Nucl. Mater.* **390** 10–9
[13] Pitts R.A. *et al* 2013 *J. Nucl. Mater.* **438** S48–56
[14] Kukushkin A.S., Pacher H.D., Pacher G.W., Kotov V., Pitts R.A. and Reiter D. 2013 *J. Nucl. Mater.* **438** S203–7
[15] Potzel S., Wischmeier M., Bernert M., Dux R., Müller H.W., Scarabosio A. and The ASDEX Upgrade Team 2014 *Nucl. Fusion* **54** 013001
[16] Kallenbach A. *et al* and The ASDEX Upgrade Team 2015 *Nucl. Fusion* **55** 053026
[17] Reimold F., Wischmeier M., Bernert M., Potzel S., Kallenbach A., Müller H.W., Sieglin B., Stroth U. and The ASDEX Upgrade Team 2015 *Nucl. Fusion* **55** 033004
[18] Giroud C. *et al* 2015 *Plasma Phys. Control. Fusion* **57** 035004
[19] Reimerdes H. *et al* and The TCV Team 2013 *Plasma Phys. Control. Fusion* **55** 124027
[20] Petrie T.W. 2013 *Nucl. Fusion* **53** 113024
[21] Soukhanovskii V.A. *et al* 2013 *J. Nucl. Mater.* **438** S96–101
[22] Vijvers W.A.J. *et al* and The TCV Team 2014 *Nucl. Fusion* **54** 023009
[23] Havlíčková E., Harrison J., Lipschultz B., Fishpool G., Kirk A., Thornton A., Wischmeier M., Elmore S. and Allan S. 2015 *Plasma Phys. Control. Fusion* **57** 115001
[24] Lunt T., Canal G.P., Duval B.P., Feng Y., Labit B., McCarthy P., Reimerdes H., Vijvers W.A.J. and Wischmeier M. 2016 *Plasma Phys. Control. Fusion* **58** 045027
[25] Ryutov D.D. 2007 *Phys. Plasmas* **14** 064502
[26] Takase H. 2001 *J. Phys. Soc. Japan* **70** 609
[27] Kotschenreuther M., Valanju P.M., Mahajan S.M. and Wiley J.C. 2007 *Phys. Plasmas* **14** 072502
[28] Valanju P.M., Kotschenreuther M., Mahajan S.M. and Canik J. 2009 *Phys. Plasmas* **16** 056110
[29] LaBombard B. *et al* 2015 *Nucl. Fusion* **55** 053020
[30] Kotschenreuther M., Valanju P., Covele B. and Mahajan S. 2013 *Phys. Plasmas* **20** 102507
[31] Lipschultz B., Parra F.I. and Hutchinson I.H. 2016 *Nucl. Fusion* **56** 056007
[32] Eich T., The ASDEX Upgrade Team and The J. EFDA Contributors 2013 *Nucl. Fusion* **53** 093031
[33] Loarte A. *et al* 1999 *J. Nucl. Mater.* **266** 587–92
[34] Eich T., Sieglin B., Scarabosio A., Fundamenski W., Goldston R.J. and Herrmann A. 2011 *Phys. Rev. Lett.* **107** 215001
[35] Makowski M.A. *et al* 2012 *Phys. Plasmas* **19** 056122
[36] Ryutov D.D., Cohen R.H., Farmer W.A., Rognlien T.D. and Umansky M.V. 2014 *Phys. Scr.* **89** 088002
[37] Ryutov D.D., Makowski M.A. and Umansky M.V. 2010 *Plasma Phys. Control. Fusion* **52** 105001
[38] Labit B. *et al* 2016 Experimental studies of the snowflake divertor in TCV *Nucl. Mater. Energy* submitted
[39] Stangeby P.C. 2000 *The Plasma Boundary of Magnetic Fusion Devices* (Bristol: Institute of Physics Publishing)
[40] Kotschenreuther M., Valanju P., Mahajan S., Zheng L.J., Pearlstein L.D., Bulmer R.H., Canik J. and Maingi R. 2010 *Nucl. Fusion* **50** 035003
[41] Loarte A. *et al* 1998 *Nucl. Fusion* **38** 331–71
[42] McIntosh S., Hancock D., Taylor D., Morris W., Surrey E., Todd T., Cunningham G. and Fishpool G. 2014 Engineering feasibility of the double Decker divertor (FIP/P8-9) *25th IAEA Int. Conf. on Fusion Energy Conf. (St Petersburg, Russian Federation, 13–18 October 2014)*
[43] Rognlien T.D., Porter G.D. and Ryutov D.D. 1999 *J. Nucl. Mater.* **266** 654–9
[44] Coda S. and The TCV Team 2015 *Nucl. Fusion* **55** 104004
[45] Fasoli A. and The TCV Team 2015 *Nucl. Fusion* **55** 043006
[46] Reimerdes H. *et al* 2016 TCV divertor upgrade for alternative magnetic configurations *Nucl. Mater. Energy* accepted
[47] Pitts R.A. *et al* and The TCV Team 2001 *J. Nucl. Mater.* **290** 940–6
[48] Wischmeier M. *et al* 2004 *Contrib. Plasma Phys.* **44** 268–73
[49] Wischmeier M. 2005 Simulating divertor detachment in the TCV, JET tokamaks *PhD Dissertation* and No. 3176, Ecole Polytechnique Federale de Lausanne
[50] Harrison J.R. *et al* 2016 Detachment dynamics on the TCV tokamak *Nucl. Mater. Energy* (http://doi.org/10.1016/j.nme.2016.10.020)
[51] Verhaegh K. *et al* 2017 Spectroscopic investigations of divertor detachment in TCV *Nucl. Mater. Energy* (http://doi.org/10.1016/j.nme.2017.01.004)

[52] Burrell K.H. 1978 *Rev. Sci. Instrum.* **49** 948–54
[53] Bates S.C. and Burrell K.H. 1984 *Rev. Sci. Instrum.* **55** 934–9
[54] Wischmeier M., Pitts R.A., Horacek J., Coster D. and Reiter D. 2005 *Proc. 32nd EPS Conf. (Tarragona, Spain, 27 June–1 July 2005)* P-5.013 (http://epsppd.epfl.ch/Tarragona/pdf/P5_013.pdf)
[55] Kruezi U., Sergienko G., Morgan P.D., Matthews G.F., Brezinsek S., Vartanian S. and The JET-EFDA Contributors 2012 *Rev. Sci. Instrum.* **83** 10D728
[56] Pitts R.A., Alberti S., Blanchard P., Horacek J., Reimerdes H. and Stangeby P.C. 2003 *Nucl. Fusion* **43** 1145–66
[57] Brezinsek S. *et al* and The JET-EFDA contributors 2009 *J. Nucl. Mater.* **390** 267–73
[58] Marki J., Pitts R.A., Eich T., Herrmann A., Horacek J., Sanchez F. and Veres G. 2007 *J. Nucl. Mater.* **363** 382–8
[59] Theiler C. 2011 Basic investigation of turbulent structures and blobs of relevance for magnetic fusion plasmas *PhD Dissertation* and No. 5228, Ecole Polytechnique Federale de Lausanne
[60] Theiler C., Furno I., Kuenlin A., Marmillod P. and Fasoli A. 2011 *Rev. Sci. Instrum.* **82** 013504
[61] Nakano T., Kubo H., Asakura N., Shimizu K., Kawashima H. and Higashijima S. 2009 *J. Nucl. Mater.* **390** 255–8
[62] Nakano T., Kubo H., Asakura N. and Shimizu K. 2009 *American Institute of Physics Conf. Series* vol **1125** pp 131–40
[63] Karpushov A.N. *et al* 2016 *Fusion Eng. Design* (https://doi.org/10.1016/j.fusengdes.2017.02.076)
[64] Gallo A. *et al* 2016 Effect of plasma geometry on divertor heat flux spreading: MONALISA simulations and experimental results from TCV *Nucl. Mater. Energy* (http://doi.org/10.1016/j.nme.2016.10.003)
[65] Covele B., Valanju P., Kotschenreuther M. and Mahajan S. 2014 *Nucl. Fusion* **54** 072006